An experimental study of the effects of rapid rotation on turbulence

By Srinivas V. Veeravalli

The effects of rotation on grid turbulence were studied in a low speed tunnel. Results are presented for both axisymmetric and non-axisymmetric flows. As observed by previous workers, the cascade process was seen to be effectively blocked by rotation leading to reduced dissipation. In the non-axisymmetric case, rotation caused the flow to tend rapidly towards axisymmetry; however, for the length studied, the flow tended to move away from isotropy. Based on the results, some recommendations are made on the design of a larger facility for studying similar flows.

1. Motivation and objectives

Experiments (Traugott, 1958, Wigeland & Nagib, 1978, and Jacquin *et al.*, 1988, 1990), large eddy simulations (Bardina *et al.*, 1985), and direct numerical simulations (Bardina *et al.*, 1985 and Speziale *et al.*, 1987) all show that rapid rotation (i.e. the rotation time scale $(1/\Omega) << $ the turbulence time scale) has a striking effect on homogeneous nearly isotropic turbulence. The cascade process is effectively inhibited by rotation, thus dissipation is greatly reduced. Some attempts have been made to incorporate this effect in turbulence models (Bardina *et al.*, 1985 and Speziale *et al.*, 1987); however, none of the present models fully account for the subtle effects of rotation. Numerical simulations further showed the somewhat surprising result that anisotropic homogeneous turbulence subjected to rotation tended towards an isotropic state; however, the residual anisotropy was not necessarily zero. Reynolds (1989) performed a detailed analysis using Rapid Distortion Theory (RDT) and showed that a reduction in the anisotropy is indeed expected, and if the anisotropy is produced by irrotational strain, then the anisotropy tensor b_{ij} is asymptotically driven to half its initial value.

Our objective was to extend the work of the experiments mentioned above to lower turbulent Rossby numbers ($R_{o\lambda} \equiv (\frac{1}{3}q^2)^{\frac{1}{2}}/(\lambda\Omega)$, where λ is the Taylor microscale and q^2 is twice the turbulent kinetic energy), and to study the effects of rotation on non-axisymmetric turbulence.

2. Previous work

Experimental studies of rotating turbulence can be broadly classified into two groups: *a*) rotating tank experiments and *b*) wind tunnel experiments.

The work of Ibbetson & Tritton (1975) and Hopfinger *et al.* (1982) belong to category *a*. Ibbetson & Tritton dropped a grid into a rotating tank and found that the turbulence behind the grid decayed much faster in the presence of rotation. Hopfinger *et al.* (1982) used a shaking grid to generate turbulence and found that

away from the grid the flow exhibited a strong tendency towards 2-dimensionality and essentially consisted of columnar vortices aligned with the axis of rotation.

Traugott (1958), Wigeland & Nagib (1978), and Jacquin *et al.* (1988, 1990), on the other hand, imposed solid body rotation on grid turbulence in a wind tunnel, thus these experiments approximate homogeneous turbulence better. The smallest value of $R_{o\lambda}$ achieved in the Wigeland & Nagib (1978) experiment was approximately 0.4 while Jacquin *et al.* (1988, 1990) obtained a value of 0.6. These experiments showed that the mildly anisotropic grid turbulence tended towards isotropy and that the kinetic energy decay was greatly reduced due to an inhibition of the cascade process. Jacquin *et al.* (1990) conducted a detailed study of length scales and showed that the length scales along the axis of rotation grew at a much faster rate compared to the non-rotating case and showed departures from the behavior expected in isotropic flow (the direct numerical simulation results of Bardina *et al.*, 1985 show a similar behavior for the length scales). However, no two-point measurements were made and all the length scales were obtained from the time series, invoking Taylor's hypothesis.

Large eddy simulations and direct numerical simulations (Bardina *et al.*, 1985 and Speziale *et al.*, 1987) also showed the dramatic suppression of the spectral transfer term observed in experiments. In particular, Speziale *et al.* (1987) found that the development of the energy spectrum $E(\underline{\kappa}, t)$ agreed extremely well with

$$E(\underline{\kappa}, t) = E(\underline{\kappa}, t_o)\, exp[-2\nu\kappa^2(t - t_o)] \tag{1}$$

which is what is expected for purely viscous decay with the spectral transfer term equal to zero. (ν is the kinematic viscosity, $\underline{\kappa}$ the wave number vector, and the development is for $t > t_o$.) Speziale *et al.* (1987) also showed that homogeneous (unbounded) turbulence does not undergo Taylor-Proudman reorganization.

3. Apparatus and instrumentation

The experiments described here were carried out in a facility similar in design to those used by Wigeland & Nagib (1978) and Jacquin *et al.*(1990). The output of standard blower tunnel consisting of a wide angle diffuser, a plenum chamber with 4 screens, and a honeycomb, followed by a contraction (8:1) section, is fed into a rotating section which is 15.24cm in diameter. The rotating section (figure 1) houses the swirl generator at the entrance and the turbulence generating grid near the exit. It consists of a cylinder mounted between slender bearings and driven by a pair of friction wheels, which are in turn driven by a 1 h.p. motor. The swirl generator consists of a layer of low density foam (8 pores per cm, 0.64cm thick) followed by a honeycomb (cell size 3.7mm and 4.0cm long) and a screen (of 0.07cm mesh size and a porosity of approximately 0.6) placed approximately 40 cell diameters downstream of the honeycomb. Circumferential velocity is imparted to the fluid mainly by the honeycomb; however, the axial velocity resulting from the use of a honeycomb alone is non-uniform because of higher blockage at the periphery due to the higher angles of flow incidence there. The use of the foam alleviates this problem since part of the swirl is imparted by the foam. Any residual inhomogeneities in the axial velocity

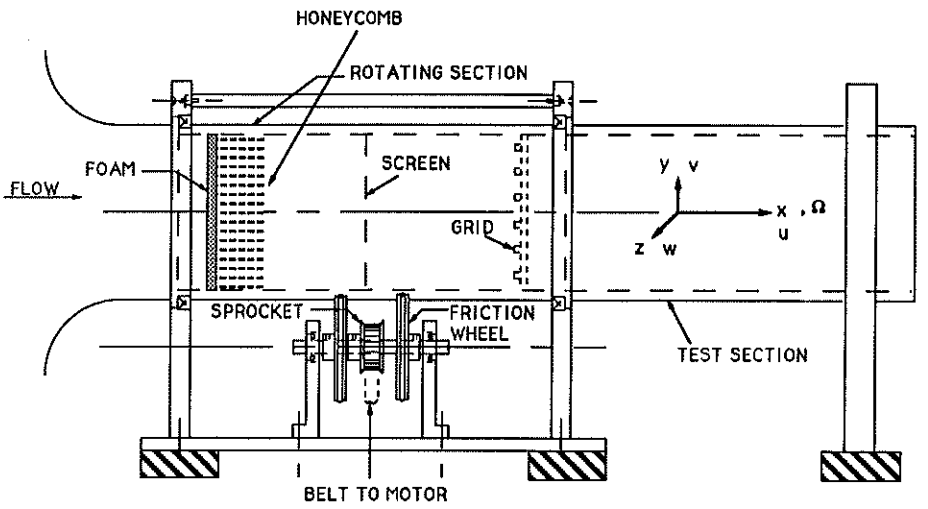

FIGURE 1. Schematic Diagram of the rotating section.

distribution are smoothed out by the screen. As shown in section 4, the resulting velocity distribution shows that the fluid is indeed in solid-body rotation away from the walls and is convected downstream with a uniform axial velocity. Measurements were made in a stationary test section approximately 1.4m long. The test section is mounted on a separate table and a small air gap ($\approx 0.5mm$) was maintained between the rotating section and the test section so that no vibrations were transmitted from the rotating section to the test section. For all the measurements described below, the turbulence generating grid consisted of a bi-planar array of square bars, with a mesh size (M) of 1cm and solidity (ratio of closed area to the total area) of 0.37.

Measurements were made with Dantec 55P51 cross-wire probes (5 μm in diameter and approximately 1mm long) operated by Microscale HWM-100 anemometers. The hot-wire signals were low-pass filtered before being digitized by a Data Translation DT2828 data acquisition board.

4. Accomplishments

Figure 1 shows the coordinate frame used in the ensuing discussions. For off-axis measurements, y denotes the radial direction and z denotes the azimuthal direction.

Figure 2 shows profiles of the mean velocity and velocity variances obtained at $x/M = 20$ and $x/M = 100$ with the cylinder spinning at approximately 1200 r.p.m. As can be seen, the swirl generator is quite successful in producing the required velocity field. Away from the wall, the axial velocity is uniform, while the azimuthal velocity varies linearly with radius. The slight spin-up that is observed at $x/M = 100$ is due to the growth of the boundary layers. At $x/M = 20$, the region where the fluctuation field is homogeneous has a diameter of approximately 10M and this drops to approximately 5M at the larger downstream distance. We

note that the variance values reported off-axis are obtained from mean values (over angle) of phase-locked averages. This procedure was necessary since small variations in the mean axial velocity with angle gave rise to fairly large spurious fluctuations since the turbulence intensity was small.

4.1 Axisymmetric turbulence

The decay of the turbulent kinetic energy, and its components, with downstream distance is shown in figure 3 for $\Omega = 0$ rad/s and $\Omega \approx 126$ rad/s. The measurements were made along the centerline. Let us first look at the behavior for x/M less than 100. We see that although the variances are nearly equal initially, for the two cases, the decay rate is much slower in the presence of rotation as was observed by Wigeland & Nagib (1978) and Jacquin *et al.* (1990). The kinetic energy decay exponent drops from 1.34 in the non-rotating case to 0.91 for Ω of 126 rad/s. As noted by previous researchers, in the presence of rotation, the spectral modes get de-coupled, thus spectral transfer is inhibited, leading to a reduced dissipation rate. A study of spectra further reveals this process. Figure 4 compares u and v spectra at $x/M = 20$ and $x/M = 60$. Initially ($x/M = 20$), the spectra for the rotating and non-rotating cases are nearly identical; however, at $x/M = 60$, the low frequency (wavenumber) energy content is higher in the presence of rotation, while the high frequency (wavenumber) energy content is lower. This is what one would expect when spectral transfer is inhibited — the low wavenumber motions would be preserved, while the high wavenumber motions would decay more rapidly since the energy lost due to viscous effects is not replaced by spectral transfer. A more detailed study of spectra and length scales will be made when two-point correlations are measured. For the present, we note that the evolution of the length scales is similar to that observed by Jacquin *et al.* (1990). Various turbulence parameters corresponding to the axisymmetric flow are presented in Table 1.

(x/M)	$k\ (m^2/s^2)$	$\epsilon\ (m^2/s^3)$	$l(cm)$	$\lambda\ (cm)$	Re_λ
20	0.191	11.8	0.71	0.16	35.9
60	0.045	0.95	1.0	0.28	30.1

TABLE 1a: Turbulence parameters for $M = 1cm$, $\Omega = 0$ and $U \approx 9.2\ m/s$.

(x/M)	$k\ (m^2/s^2)$	$\epsilon\ (m^2/s^3)$	$l(cm)$	$\lambda\ (cm)$	Re_λ	Ro_λ
20	0.202	8.13	1.12	0.20	45.6	1.46
60	0.081	1.13	2.04	0.34	49	0.54

TABLE 1b: Turbulence parameters for $M = 1cm$, $\Omega = 126\ rad/s$ and $U \approx 9.5\ m/s$.

Let us now examine the behavior for x/M greater than 100, in figure 3. We see that $\overline{u^2}$ becomes nearly constant, while $\overline{v^2}$ actually increases with increasing downstream distance. To examine this phenomenon in greater detail, centerline measurements were made without the grid at different rotation rates. Figure 5

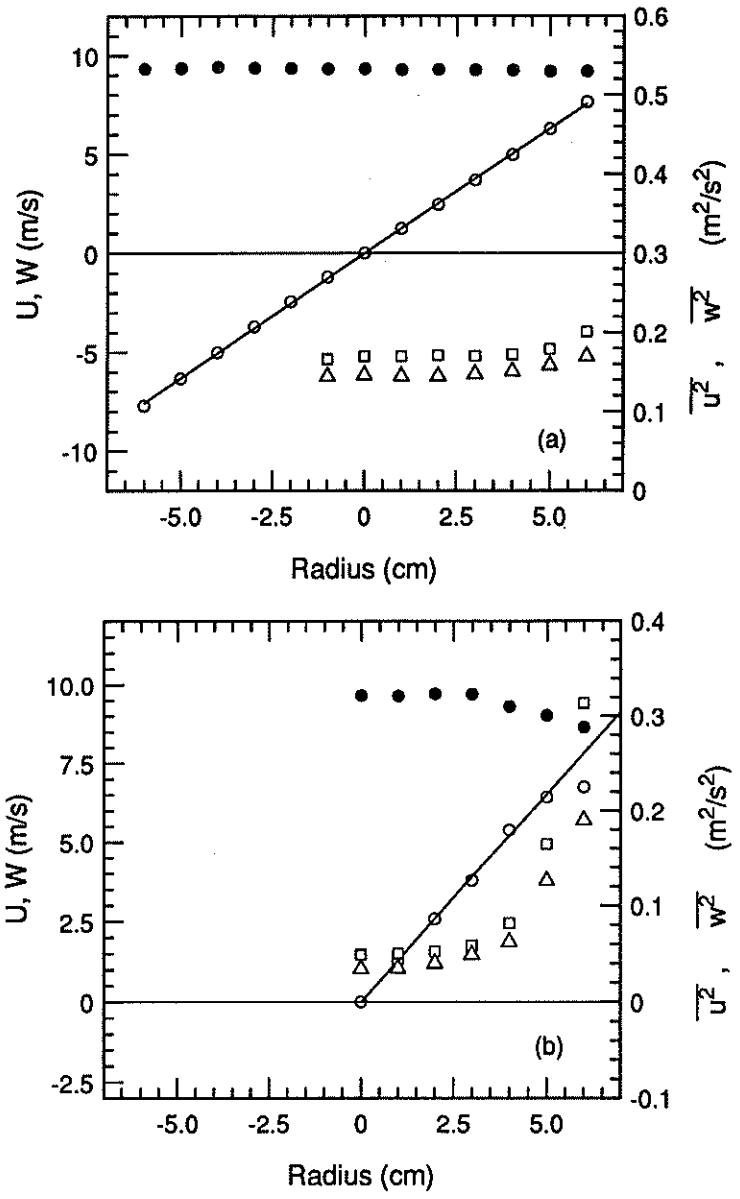

FIGURE 2. Mean velocity and variance profiles at; a) $x/M = 20$ and b) $x/M = 100$. The symbols are: • U; ○ W; □ $\overline{u^2}$ and △ $\overline{w^2}$. The straight line fit to the azimuthal velocity data in a) has a slope corresponding to 126 rad/s and in b) the slope is 130.6 rad/s.

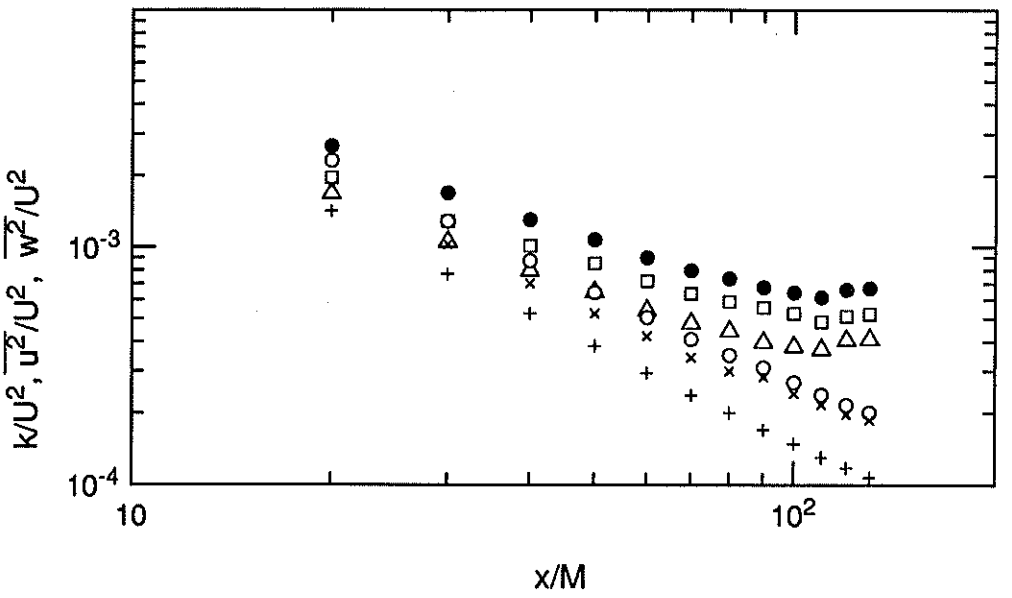

FIGURE 3. Decay of normalized variances and kinetic energy with and without rotation. The symbols are: 1) $\Omega = 126 rad/s$, • k/U^2; □ $\overline{u^2}/U^2$; △ $\overline{w^2}/U^2$ and 2) $\Omega = 0$, ○ k/U^2; × $\overline{u^2}/U^2$; + $\overline{w^2}/U^2$

shows the evolution of the turbulent kinetic energy for various rotation rates. We see that k increases dramatically beyond a certain x in each of the three cases with rotation. The mean velocity profiles indicate that there is no turbulence production in the region near the center, thus the data is contaminated by boundary effects — originating either from the side wall or from the exit. To examine if end effects were propagating upstream, the end condition (for $\Omega = 126$ rad/s) was modified in two ways: a) the test section was lengthened by 20% and b) an obstruction (grid) was placed at the exit. In either case, the results were identical to those shown in figure 5. Thus, the contamination of the centerline data is due to disturbances originating from the cylinder wall. It can be shown that the contribution of irrotational fluctuations originating from the edge of the boundary layer is at least three orders of magnitude smaller than the observed levels, thus the increase in centerline intensity is due to the propagation of the boundary layer fluctuations in the form of inertial waves. The speed of propagation of these waves is proportional to the size of the disturbance and to the rotation rate (Greenspan, 1968). The size of the disturbance is approximately constant between the three rotation rates — the boundary layer thickness (δ_{99}) varies by approximately 30% for the three rotation rates. Thus, assuming that the growth of the boundary layer is linear, it can be shown that the downstream location at which the waves originating from the boundary reach the center should vary approximately as $\Omega^{-\frac{1}{2}}$. This is consistent with the behavior seen in figure 5.

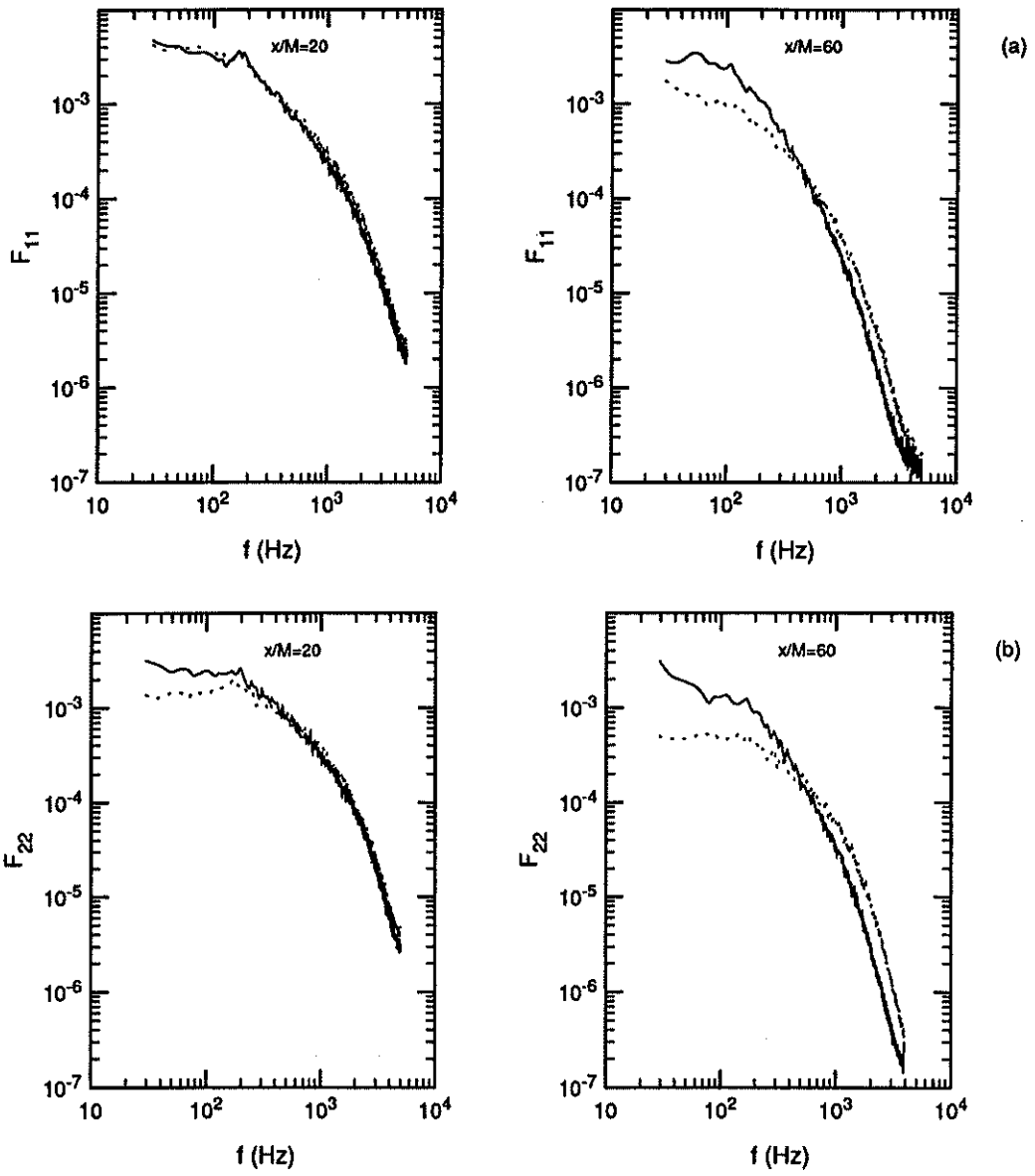

FIGURE 4. Comparison of a) u-spectra (F_{11}) and b) v-spectra (F_{22}) with and without rotation. ——, $\Omega = 126 rad/s$; and ····· , $\Omega = 0 rad/s$. The vertical scale is arbitrary.

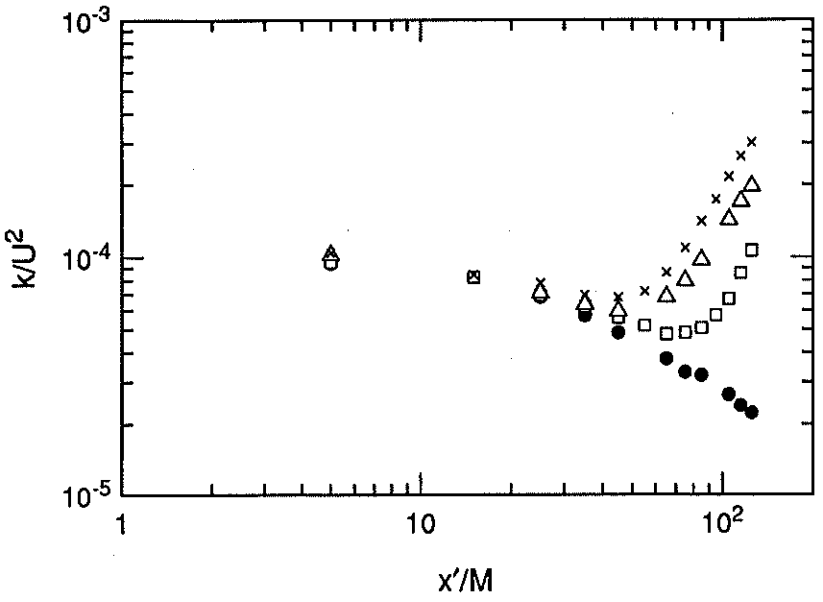

FIGURE 5. Behavior of the background fluctuations for different rotation rates. • $\Omega = 0$; □ $\Omega = 53 rad/s$; △ $\Omega = 93 rad/s$; and × $\Omega = 126 rad/s$. (x' denotes the distance from the start of the test section.)

4.2 Non-axisymmetric turbulence

A number of different mono-planar grids with rectangular bars of various aspect ratios were tested in an effort to generate non-axisymmetric homogeneous turbulence, without much success. We finally decided to use a bi-planar grid to generate homogeneous nearly isotropic turbulence and modify it with an array of vanes, placed within the rotating section, to introduce the non-axisymmetry. A schematic view of this arrangement is shown in figure 6. (Note that y now denotes the direction perpendicular to the vanes and z is parallel to the vanes.) Various chord sizes, (c), and vane spacings, (d), were tried, and it was found that a spacing of 1.5cm and a chord size of 1.27cm yielded the best results with the 1cm mesh grid. Even with this optimal configuration, the resulting non-axisymmetry was not large — $\overline{w^2}$ was at most 30% larger than $\overline{v^2}$.

Figure 7 shows the variation of the principal Reynolds stresses in the y and z directions at $x/M = 25$ and $x/M = 105$ for the case without rotation. We see that the flow is reasonably homogeneous in the core region. The smaller x/M corresponded to a distance of 10 vane spacings from the vane array, thus, in those measurements, the uniformity is better in the z direction than in the y direction.

The evolution of the normalized variances $\overline{u^2}/U^2$, $\overline{v^2}/U^2$ and $\overline{w^2}/U^2$, is shown in figure 8 with and without rotation. The background turbulence levels shown in figure 5 were subtracted in each case. This caused the a drop in variance of

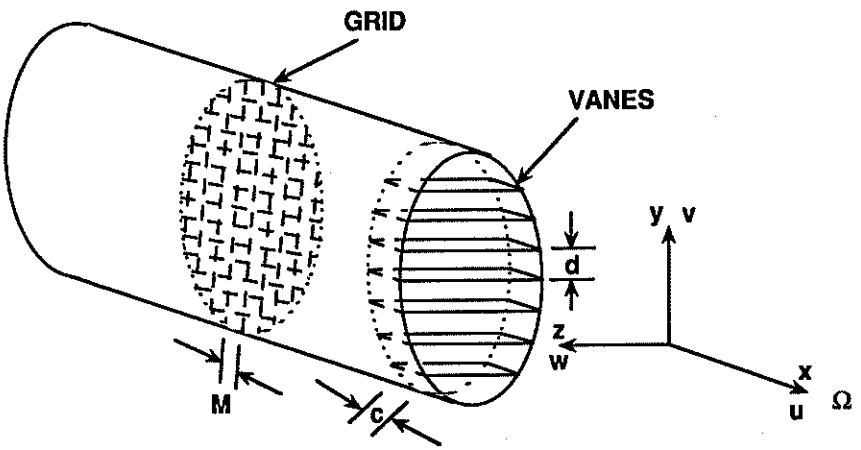

FIGURE 6. Schematic view of the non-axisymmetric-turbulence generator.

approximately 20% in the worst case (largest x/M), but the qualitative features of the curves remained unchanged. The various turbulence parameters corresponding to these flows are given in table 2. Just as in the axisymmetric case, the decay is much slower in the presence of rotation. We also note that while $\overline{v^2}$ and $\overline{w^2}$ remain distinct in the non-rotating case, they are nearly equal in the rotating case.

(x/M)	$k\ (m^2/s^2)$	$\epsilon\ (m^2/s^3)$	$l(cm)$	$\lambda\ (cm)$	Re_λ
20	0.178	11.49	0.66	0.17	39.6
60	0.037	0.80	0.9	0.30	32.4
100	0.019	0.26	1.04	0.38	30.0

TABLE 2a: Turbulence parameters for $M = 1cm$, $\Omega = 0$ and $U \approx 9.2\ m/s$.

(x/M)	$k\ (m^2/s^2)$	$\epsilon\ (m^2/s^3)$	$l(cm)$	$\lambda\ (cm)$	Re_λ	Ro_λ
20	0.17	7.96	0.87	0.19	42.5	1.92
60	0.056	0.9	1.49	0.26	45.3	.64
100	0.037	0.37	1.91	0.32	47.7	0.41

TABLE 2b: Turbulence parameters for $M = 1cm$, $\Omega = 93\ rad/s$ and $U \approx 9.3\ m/s$.

In both the flows, all six Reynolds stresses were measured. In the absence of rotation, this was achieved by choosing four orientations of the vanes such that the instantaneous cross stream velocity measured was $(w - v)/\sqrt{2}$, w, $(w + v)/\sqrt{2}$

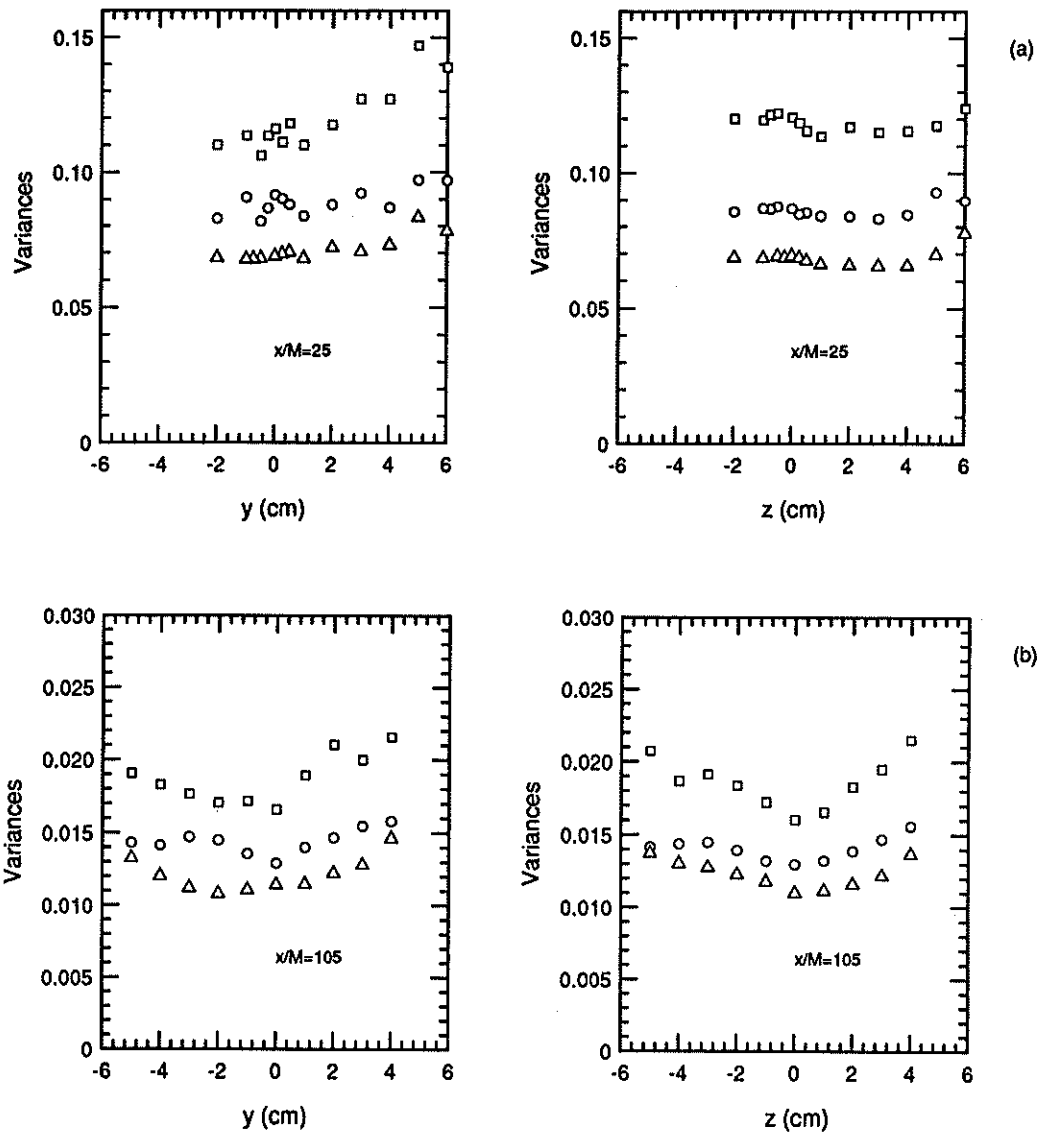

FIGURE 7. Variation of the velocity variances in the transverse plane (non-axisymmetric turbulence). a) $x/M = 25$ and b) $x/M = 105$. The symbols are: □ $\overline{u^2}$; △ $\overline{v^2}$; and ○ $\overline{w^2}$.

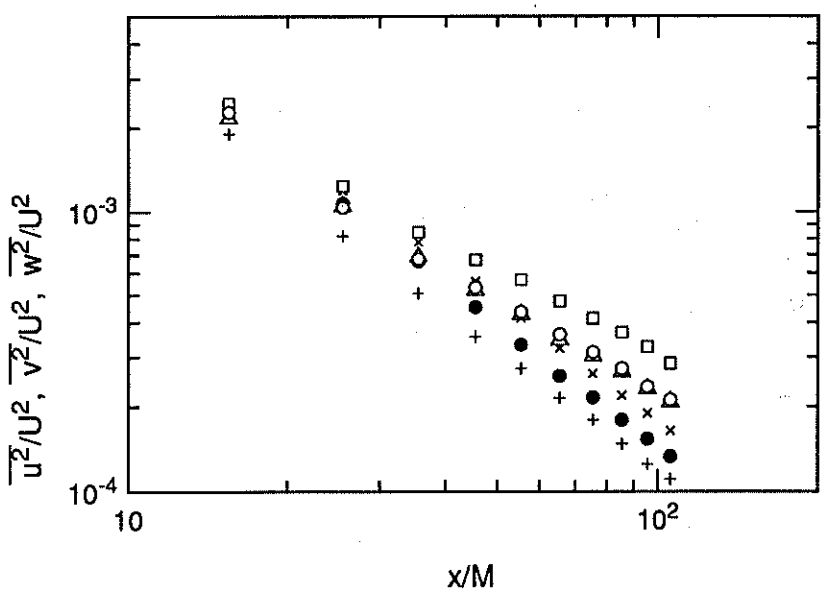

FIGURE 8. Evolution of the velocity variances (non-axisymmetric turbulence).The symbols are:1) $\Omega = 93 rad/s$, □ $\overline{u^2}/U^2$; △ $\overline{v^2}/U^2$; ○ $\overline{w^2}/U^2$ and 2) $\Omega = 0$, × $\overline{u^2}/U^2$; + $\overline{v^2}/U^2$; • $\overline{w^2}/U^2$

and v respectively. In the rotating case, the stresses in the transverse plane were obtained by fitting sine functions to phase-locked averages. This procedure is shown in figure 9. (Here, z lags the trigger by 33°, thus $\overline{w^2}$ is obtained when θ is 33° and $\overline{v^2}$ corresponds to θ of 123°.) For comparison, a similar distribution obtained from the axisymmetric case is also shown. The data in figure 9a are clearly well represented by the best-fit sine curve with a period of 180°, while the data in figure 9b do not exhibit any such trend. The larger scatter in figure 9b is due to the fact that a smaller number of samples was used in computing these averages.

The evolution of $\overline{w^2}/\overline{v^2}$, the ratio of the principal stresses in the transverse plane, σ_1^2/σ_2^2, and $2\overline{u^2}/(\overline{v^2}+\overline{w^2})$ are shown in figure 10. Figure 10a shows the non-rotating case. Here σ_1^2/σ_2^2 increases to approximately 1.3 initially, then decays to approximately 1.2 and then remains nearly constant. Further, σ_1^2/σ_2^2 is almost identical to $\overline{w^2}/\overline{v^2}$ throughout, indicating that the principal directions remain approximately fixed. The ratio $2\overline{u^2}/(\overline{v^2}+\overline{w^2})$ also increases initially and then remains nearly constant. The overall behavior is consistent with that observed in grid-turbulence, wherein the tendency towards isotropy is slight for the small anisotropies encountered (Comte-Bellot & Corrsin, 1966).

The evolution is quite different in the presence of rotation as shown in figure 10b. Here, $\overline{w^2}$ and $\overline{v^2}$ are nearly equal throughout. However, the principal stresses are not equal and their ratio increases initially to approximately 1.2 before decaying to a value close to 1 at the end of the test section. Barring the last data point, the value of $2\overline{u^2}/(\overline{v^2}+\overline{w^2})$ seems to increase steadily with downstream distance.

The behavior described above is summarized in figure 11, where the evolution

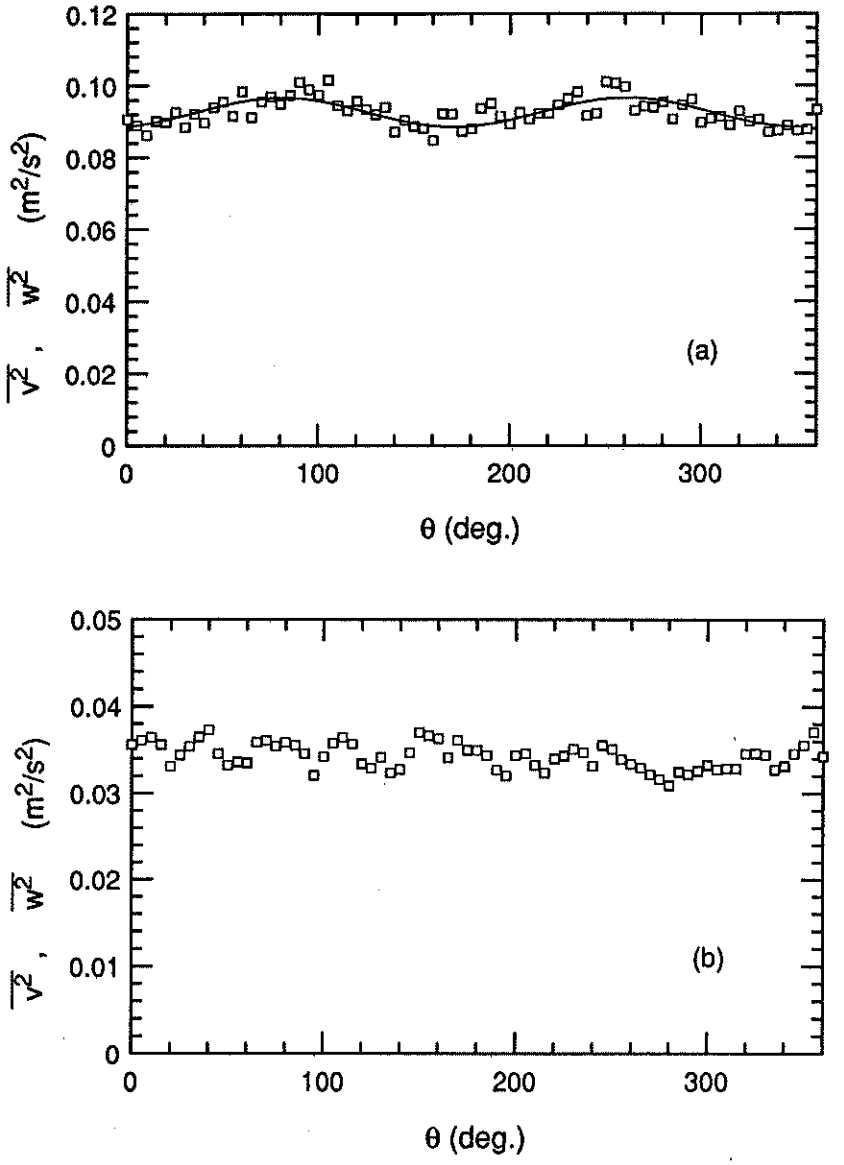

FIGURE 9. Typical plots of the variation of the transverse velocity component with angle. a) Non-axisymmetric turbulence, $\Omega = 93 rad/s$ and b)axisymmetric turbulence, $\Omega = 126 rad/s$. The solid line in figure a) is a best fit sinusoid.

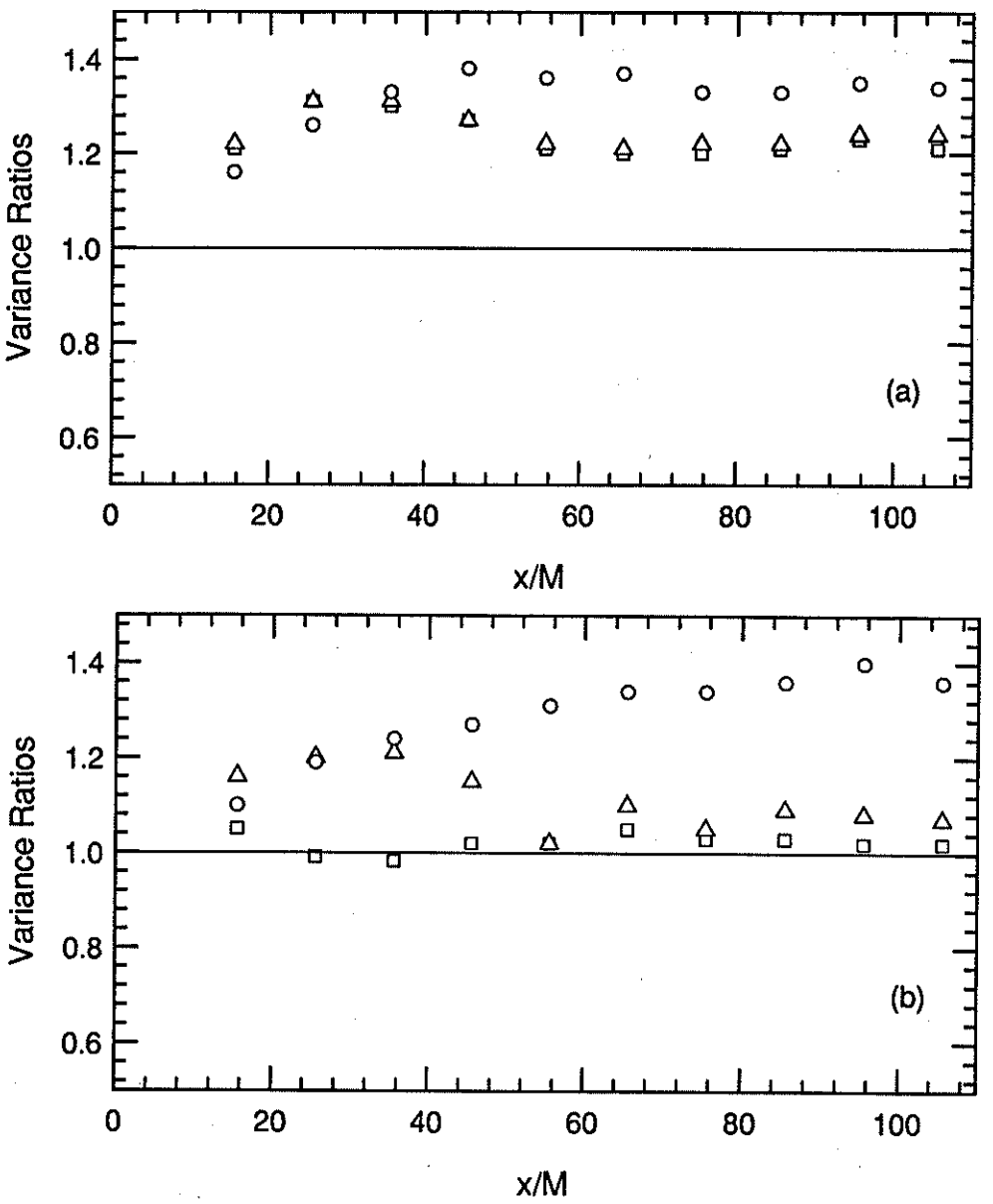

FIGURE 10. Evolution of the variance ratios (non-axisymmetric turbulence). a) $\Omega = 0$ and b) $\Omega = 93 rad/s$. The symbols are : o $2\overline{u^2}/(\overline{v^2} + \overline{w^2})$; □ $\overline{w^2}/\overline{v^2}$; and △ σ_1^2/σ_2^2.

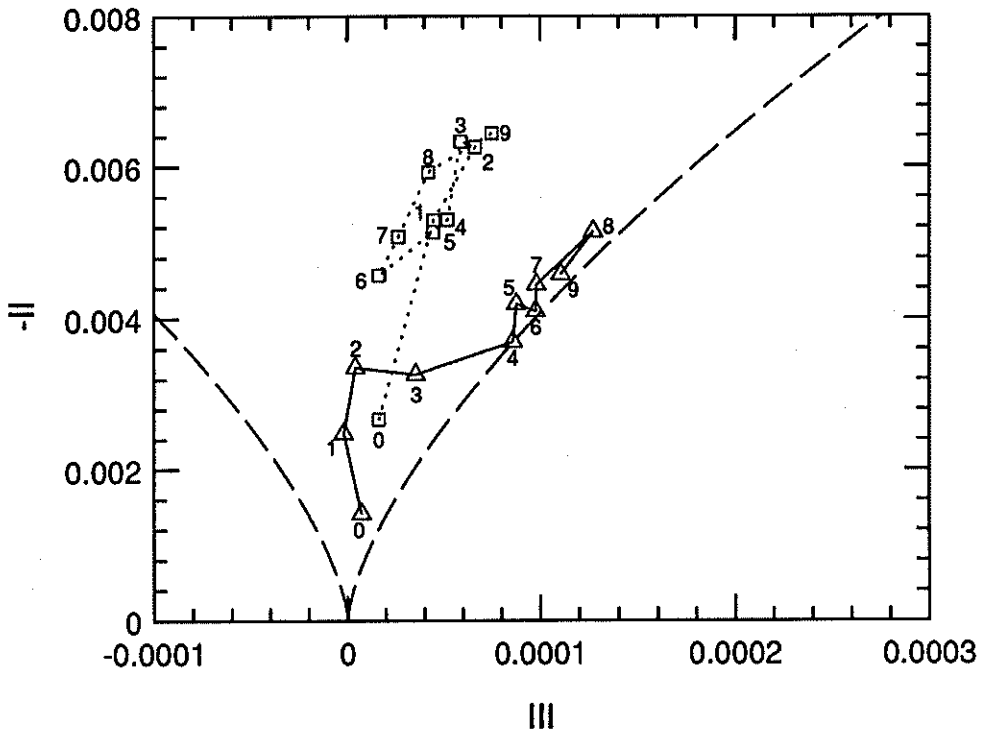

FIGURE 11. Evolution of non-axisymmetric turbulence on the II, III plane. □ $\Omega = 0$ and △ $\Omega = 93 rad/s$. The numbers alongside the symbols indicate the downstream position starting with $x/M = 10$ and ending at $x/M = 100$. (Note, the numbers start at 0 and end at 9.)

is studied on the II, III map. (II and III refer to the second and third invariants of the anisotropy tensor $b_{ij} \equiv (\overline{u_i u_j} - \overline{u_i u_i}\delta_{ij}/3)/\overline{u_i u_i}$, respectively.) We note that the values of II and III are very small and obtained from small differences of the variances, thus the error bars are very large. Indeed, the data points changed by as much 25% between different runs and for slightly different (the changes in the variances were less than 1%) hot-wire calibrations. However, the topological features of the curves remained unchanged, and we are confident that the qualitative behavior has been captured quite accurately. We see that in the absence of rotation there is initial region of development wherein the curve rapidly moves away from the isotropic point, after which the data points cluster around ($5\text{x}10^{-5}$,$-5.5\text{x}10^{-3}$). With rotation, however, after the initial departure from the isotropic point, the curve swings sharply towards the axisymmetry line and, except for the last data point, seems to climb up along it.

The equations governing the evolution of the Reynolds stresses in a co-ordinate system rotating with the swirl generator (assuming homogeneity) are:

$$U\frac{\partial\overline{u^2}}{\partial x} = \frac{2}{\rho}\overline{p\frac{\partial u}{\partial x}} + 2\nu\overline{\frac{\partial u}{\partial x_j}\frac{\partial u}{\partial x_j}}, \tag{2}$$

$$U\frac{\partial\overline{v^2}}{\partial x} = \frac{2}{\rho}\overline{p\frac{\partial v}{\partial y}} + 4\Omega\overline{vw} + 2\nu\overline{\frac{\partial v}{\partial x_j}\frac{\partial v}{\partial x_j}}, \tag{3}$$

$$U\frac{\partial\overline{w^2}}{\partial x} = \frac{2}{\rho}\overline{p\frac{\partial w}{\partial z}} - 4\Omega\overline{vw} + 2\nu\overline{\frac{\partial w}{\partial x_j}\frac{\partial w}{\partial x_j}}, \tag{4}$$

and

$$U\frac{\partial\overline{vw}}{\partial x} = \frac{1}{\rho}\overline{p\left(\frac{\partial v}{\partial z} + \frac{\partial w}{\partial y}\right)} + 2\Omega(\overline{w^2} - \overline{v^2}) + 2\nu\overline{\frac{\partial v}{\partial x_j}\frac{\partial w}{\partial x_j}}. \tag{5}$$

If we look only at the terms containing Ω, then we see that initially $\overline{vw}$ increases (since $\overline{w^2}$ is larger than $\overline{v^2}$), and this causes $\overline{v^2}$ to increase and $\overline{w^2}$ to decrease, thereby causing them to equalize as the data shows. We can go one step further and evaluate the principal stresses (in the transverse plane) as:

$$\sigma_1^2 = \frac{\overline{w^2} + \overline{v^2}}{2} + \left(\left(\frac{\overline{w^2} - \overline{v^2}}{2}\right)^2 + \overline{vw}^2\right)^{\frac{1}{2}}, \tag{6}$$

and

$$\sigma_2^2 = \frac{\overline{w^2} + \overline{v^2}}{2} - \left(\left(\frac{\overline{w^2} - \overline{v^2}}{2}\right)^2 + \overline{vw}^2\right)^{\frac{1}{2}}, \tag{7}$$

We can then write the evolution equations for σ_1^2 and σ_2^2 by differentiating both sides of equations (6) and (7) by x and substituting for the terms on the r.h.s. from equations (3), (4), and (5) (these are presented in the Appendix). It can then be shown that in the evolution equations for σ_1^2 and σ_2^2, the terms containing Ω cancel out exactly! Thus, we see that the terms proportional to Ω in equations (3), (4), and (5) are responsible only for the rotation of the principal directions, while the principal stresses are equalized by the pressure-strain terms which are subtly but significantly modified by rotation.

5. Future plans

We now have a fairly good understanding of the capabilities of the preliminary rig. The next step would be to study the development of both axisymmetric and non-axisymmetric turbulence over a range of Reynolds numbers and Rossby numbers by varying the mesh size and rotation rate. Two-point measurements would also be made to compare $R_{33}(r,0,0)$ and $R_{33}(0,r,0)$ so as to address the tendency towards two-dimensionality at intermediate Rossby numbers seen in the single point measurements of Jacquin *et al.*(1990).

5.1 Recommendations for rig II

Under rapid rotation, grid-generated turbulence decays approximately as

$$k = A\,U^2\left(\frac{x}{M}\right)^{-1}, \tag{8}$$

thus the dissipation term evolves as

$$\epsilon = \frac{A\,U^3}{M}\left(\frac{x}{M}\right)^{-2}. \tag{9}$$

Thus Re_λ and Ro_λ are given by

$$Re_\lambda = \sqrt{\frac{20A}{3\nu}}\,(U\,M)^{\frac{1}{2}}, \tag{10}$$

and

$$Ro_\lambda = \sqrt{\frac{A}{15\nu}}\,\frac{U^{\frac{3}{2}}\,M^{\frac{1}{2}}}{\Omega\,x}. \tag{11}$$

As noted in section 4.2, the maximum uncontaminated length of the test section is proportional to $\Omega^{\frac{1}{2}}$. More specifically, one can write

$$x_{max} \approx \sqrt{\frac{R\,U}{C\,b\,\Omega}}, \tag{12}$$

where R is the radius of the duct, b is the rate of growth of the boundary layer ($\partial\delta/\partial x$, assumed to be constant with x and ω), and C is a constant. Thus*,

$$\left(Ro_\lambda\right)_{min} = \frac{1}{2}\sqrt{\frac{A\,C\,b}{15\nu}}\,(U\,M)^{\frac{1}{2}}. \tag{13}$$

Hence, if we want to lower the Ro_λ for a fixed Re_λ (i.e. fixed UM), we have to reduce b. One option would be to spin the test section also — the data indicate that at the highest rotation rate examined, the boundary layer is twice as thick as in the non-rotating case. However, the gains from this method are more than offset by the complexity in making measurements. With hot-wires, the probes would have to be mounted on a sting extending the length of the test section, and this would definitely contaminate the measurements. With LDV systems, one would either need an optically-perfect transparent test section or a system with a focal length in excess of 1m (an LDV system with a 10-20m focal length is described in Reinath,

* Note that we have used the constraint $(\Omega R)/U \leq 1$, since, if this is violated, the vortex exiting the test-section could break down (Dellenback *et al.*,1988), thus generating a disturbance with a sufficiently large scale and, therefore, sufficiently large propagation velocity as to cause disturbances upstream of the exit. This is confirmed by the data of Jacquin *et al.*, (1990) for very large Ω.

1989, but it is expensive and shows more scatter than hot-wire measurements). The other option is to reduce the growth of the boundary layers through suction. Since the peripheral pressure is increased by rotation, one could expect a moderate reduction in boundary layer growth by simply making the test-section walls porous and perhaps adding a pressure drop device like a honeycomb at the end of the test-section to increase the bulk gauge pressure inside the test-section. However, to permit better control, the test section would have to be enclosed in another chamber connected to a fan which would provide the suction. Although increasing the diameter would not yield much benefit in terms of Rossby number, the facility would lend itself more readily to two-point measurements and would also permit us to examine higher Re flows, albeit at the price of higher Rossby numbers.

Additionally, although we have been reasonably successful in generating non-axisymmetric homogeneous turbulence, the departures from axisymmetry are not large. One could conceivably achieve larger departures by using two sets of vanes in tandem (experiments on drag reduction with LEBU's indicate that the optimal configuration is one with two plates in tandem, separated by approximately 7 chord widths, Savill, 1989). Thus, the rotating section should be long enough to permit such an arrangement.

Acknowledgements

I wish to thank Prof. Bradshaw for his helpful comments and suggestions through all the stages of this work, and in particular, for suggesting the use of a 'one-dimensional honeycomb' to generate non-axisymmetric homogeneous turbulence.

Appendix

The principal stresses are given by

$$\sigma_{1,2}^2 = \frac{\overline{w^2}+\overline{v^2}}{2} \pm \left(\left(\frac{\overline{w^2}-\overline{v^2}}{2}\right)^2 + \overline{vw}^2\right)^{\frac{1}{2}}. \tag{A1}$$

Thus,

$$\begin{aligned} U\frac{\partial \sigma_{1,2}^2}{\partial x} &= \frac{U}{2}\frac{\partial}{\partial x}\left(\overline{v^2}+\overline{w^2}\right) \pm \frac{U\left[\frac{1}{4}\left(\overline{w^2}-\overline{v^2}\right)\left(\frac{\partial \overline{w^2}}{\partial x}-\frac{\partial \overline{v^2}}{\partial x}\right)+\overline{vw}\,\frac{\partial \overline{vw}}{\partial x}\right]}{\left(\left(\frac{\overline{w^2}-\overline{v^2}}{2}\right)^2+\overline{vw}^2\right)^{\frac{1}{2}}} \\ &\approx \frac{1}{\rho}\overline{p\left(\frac{\partial v}{\partial y}+\frac{\partial w}{\partial z}\right)} + \nu\overline{\left(\frac{\partial v}{\partial x_j}\frac{\partial v}{\partial x_j}+\frac{\partial w}{\partial x_j}\frac{\partial w}{\partial x_j}\right)} \\ &\quad \pm \frac{\left(\overline{w^2}-\overline{v^2}\right)\left[\frac{1}{2\rho}\left(\overline{p\frac{\partial w}{\partial z}}-\overline{p\frac{\partial v}{\partial y}}\right)\right]+\frac{\overline{vw}}{\rho}\overline{p\left(\frac{\partial v}{\partial z}+\frac{\partial w}{\partial y}\right)}}{\left(\left(\frac{\overline{w^2}-\overline{v^2}}{2}\right)^2+\overline{vw}^2\right)^{\frac{1}{2}}}. \end{aligned} \tag{A2}$$

REFERENCES

BARDINA, J., FERZIGER, J. H. & ROGALLO, R. S. 1985 Effect of rotation on isotropic turbulence: computation and modeling. *J. Fluid Mech.* **154**, 321-336.

COMTE-BELLOT, G. & CORRSIN, S. 1966 The use of a contraction to improve the isotropy of grid generated turbulence. *J. Fluid Mech.* **25**, 657-682.

DELLENBACK, P. A., METZGER, D. E. & NEITZEL, G. P. 1988 Measurements in turbulent swirling flow through an abrupt axisymmetric expansion. *AIAA Journal.* **26**, No.6, 669-681.

GREENSPAN, H. P. 1968 *The theory of rotating fluids.* Cambridge University Press.

HOPFINGER, E. J., BROWAND, F. K. & GAGNE, Y. 1982 Turbulence and waves in a rotating tank. *J. Fluid Mech.* **125**, 505-534.

IBBETSON, A. & TRITTON, D. 1975 Experiments on turbulence in a rotating fluid. *J. Fluid Mech.* **68**, 639-672.

JACQUIN, L., LEUCHTER, O. & GEFFROY, P. 1988 Experimental study of homogeneous turbulence in the presence of rotation. *Turbulent Shear Flows 6*,ed. by L.T.S. Bradbury *et al.*, 46-57.

JACQUIN, L., LEUCHTER, O., CAMBON, C. & MATHIEU, J. 1990 Homogeneous turbulence in the presence of rotation. *J. Fluid Mech.* In press.

PHILLIPS, O. M. 1963 Energy transfer in rotating fluids by reflection of inertial waves. *Phys. Fluids.* **6**, 513-520.

REINATH, M. S. 1989 A long-range laser velocimeter for the national full-scale aerodynamics complex: new developments and experimental application. *NASA TM 101081.*

REYNOLDS, W. C. 1989 Effects of rotation on homogeneous turbulence. *Proc.* $10^{\underline{th}}$ *Australian Fluid Mech. Conf., University of Melbourne, Dec. 11- 15.*

SAVILL, A. M. 1989 The effect of an adverse pressure gradient on the drag reduction performance of manipulators. *Int. J. Heat and Fluid Flow.* **10**, No. 2, 118-124.

SPEZIALE, C. G., MANSOUR, N. N. & ROGALLO, R. S. 1987 Decay of turbulence in a rapidly rotating frame. *In Studying Turbulence Using Numerical Simulation Databases.* Proc. 1987 Summer Program, Center for Turbulence Research, Stanford U., Report CTR-S87,*205-212.*

TRAUGOTT, S. C. 1958 Influence of solid-body rotation on screen-produced turbulence. *NACA Tech. Note 4135.*

WIGELAND, R. A. & NAGIB, H. M. 1978 Grid-generated Turbulence with and without rotation about the streamwise direction. *IIT Fluids and Heat Transfer Rep.* **R78-1**, Illinois Inst. of Tech., Chicago, Illinois.